Evidencing size-dependent cooperative effects on spin crossover nanoparticles following their HS→LS relaxation

Teresa Delgado, Cristian Enachescu, Antoine Tissot, Andreas Hauser, Laure Guénée, Céline Besnard

Evidencing size-dependent cooperative effects on spin crossover nanoparticles following their HS→LS relaxation.

Teresa Delgado,[a] Cristian Enachescu,[b] Antoine Tissot,*[c] Andreas Hauser,[a] Laure Guénée[d] and Céline Besnard*[d]

The HS→LS relaxation at cryogenic temperatures after photo-excitation through the light-induced excited spin-state trapping (LIESST) effect of the $[Fe(pz)Pt(CN)_4]$ micro- and nanoparticles is probed by optical-absorption spectroscopy and X-Ray Powder Diffraction (XRPD) using synchrotron radiation. A size dependence of the relaxation mechanism is evidenced, due to the inhibition of cluster formation for smaller size particles. This result is explained by simulations performed in the frame of the mechanoelastic model.

Introduction

Spin-crossover (SCO) compounds are prototypical switchable materials presenting different magnetic, optical, electrical and structural properties depending on their electronic configuration that can switch from low spin (LS) to high spin (HS) and vice versa by changes of the temperature,[1] pressure,[2] magnetic fields[3] and also by light irradiation.[4-6] The spin transition can be followed by different techniques according to the physical properties changing during the transition: magnetic susceptibility measurements,[7-8] Mössbauer,[9-11] UV-Vis-NIR[12-16] and vibrational spectroscopies,[17] X-ray diffraction,[18-22] heat capacity measurements,[17] magnetic resonance,[23] fluorescence[24-25], etc. The spin-crossover phenomenon is observed with d^4 - d^7 transition metal ions with octahedral coordination spheres.[26] The case of Fe(II) is of interest since, when changing the electronic configuration from the diamagnetic LS $^1A_{1g}$ ($t_{eg}^6e_g^0$) to the paramagnetic HS $^5T_{2g}$ ($t_{eg}^4{}_{eg}^2$) state, two electrons move into the e_g orbitals, which have a strongly antibonding character. Thus, the metal-ligand (usually nitrogen atom) bond length increases by $\Delta r_{HL} = r_{HS} - r_{LS} = 0.2$ Å and therefore, important structural changes occur during the transition.[4, 27]

In a molecular crystal, the spin crossover complexes are interacting through H-bonding, π-π stacking, dipole-dipole, Coulomb or van der Waals interactions, while in coordination polymers the spin carrying centres are linked by much stronger coordination bonds. The coupling between the large structural changes occurring during the spin transition with strong intermolecular interactions is often invoked to explain cooperative phenomena observed in the solid state, such as abrupt thermal spin transitions with the opening of a hysteresis loop. However, strong interactions do not necessarily imply a cooperative transition. In fact, cooperativity arises from the sum of all different intermolecular interactions and steric contacts in the crystal lattice but also from the mechanical properties of the whole solid. Such effects can be explained by elastic interactions, often treated in the frame of the mean-field approximation.[5,28] Theoretical models have also been developed in order to provide a microscopic view of cooperative phenomena.[5,28-34] These models predict that in the case of strongly cooperative systems, nucleation-growth processes may occur.[31,35-36] From the experimental point of view, a complete description of the structure in both the HS and LS states is necessary in order to understand the cooperativity in a given system. Single crystal X-Ray diffraction is widely used for such purposes, as well as for investigating the dynamics of the compounds during the spin transition. For example, the coexistence of pure LS and HS phase during the thermal transition was evidenced, indicating nucleation-growth processes during the thermal transition.[37] X-Ray powder diffraction (XRPD) can also be used in order to probe structures of materials only available as microcrystals.[38] For example, the structural investigation of the HS→LS relaxation dynamics of the porous coordination polymer $[Fe(pz)Pt(CN)_4]\cdot 2.6H_2O$ (pz = pyrazine) microcrystalline powder by synchrotron-radiation-based XRPD at 15 K after a quantitative LS→HS photoexcitation was reported.[19] Sigmoidal relaxation curves were observed, arising from two different HS→LS mechanisms: a random HS→LS conversion at the beginning of the relaxation, followed by a nucleation and growth process once a critical LS fraction is reached.

Within the past ten years, the synthesis of spin crossover nanoparticles based on coordination frameworks has been widely investigated, aiming at evaluating their potential as memory storage devices. Upon size reduction, the thermal transition often becomes incomplete due to the fraction of surface sites. Indeed, the centres on the surface have different coordination and usually weaker ligand field strengths than the ones in the particle core and are therefore more likely to remain in the HS state even at low temperatures. In addition, the cooperativity is often partially lost leading to more gradual transitions and narrower hysteresis loops compared to the bulk material.[39-42] In this context, Hofmann-type SCO nanoparticles have been widely studied. Square-shaped $[Fe(pz)Pt(CN)_4]$ nanocrystals of 230×230×55 nm^3 and 61×61×20 nm^3 have successfully been synthesized by Boldog *et al.*[43] They display a rather steep thermal spin transition shifted to lower critical temperatures with respect to the bulk with a small remaining HS fraction at low temperature. Volatron *et al.*[44]

have synthesized smaller square-shaped $[Fe(pz)Pt(CN)_4]$ nanoparticles of 7 and 14 nm edge lengths with a spin transitions considerably more gradual compared to the bulk and significant remaining HS fractions at low temperature. Interestingly, the transition of the 14 nm particles still shows a hysteresis loop of 6 K. More recently Peng *et al.*[9] proved that very small $[Fe(pz)Ni(CN)_4]$ nanoparticles of few nm exhibit higher transition temperatures than bigger 12 nm samples and that in the case of the 2 nm particles, the hysteresis loop reappears thanks to the use of a NaAOT matrix, which changes the elastic properties of the system and increases the cooperativity. Therefore, the effect of size reduction on the cooperative effects in SCO systems is not straightforward and requires more attention. Indeed, while this effect is experimentally well documented and explained in the frame of several theoretical models, no direct evidence of the size dependence of cooperative interactions has been reported so far.

Herein the HS→LS relaxation at cryogenic temperatures following the light-induced excited spin-state trapping (LIESST) effect of the $[Fe(pz)Pt(CN)_4]$ in bulk and nanoparticle form is investigated by X-ray powder diffraction and simulated using the mechanoelastic model, in order to elucidate the mechanism by which the relaxation proceeds at low temperature and to establish the limiting size above which nucleation-growth mechanisms responsible of the cooperativity are relevant.

Results and discussion

Synthesis and thermal spin transition. of $[Fe(pz)Pt(CN)_4]$ nanoparticles.

Six different batches of solvent free $[Fe(pz)Pt(CN)_4]$ nanoparticles with different sizes were synthetized by the reverse micelle technique, according to the already published procedures (see Table S1 and experimental section for more details).[43] The shape and the size of the particles were determined by transmission electron microscopy (TEM) and compared to the bulk sample obtained by fast precipitation.[45] As shown in Figure 1, all the submicrometric samples consist of perfectly square-shaped very thin platelets, having an aspect ratio going from 5 to 11 depending on the size. The thickness of the 32 nm and 50 nm particles is somewhat difficult to establish precisely because most of the particles are lying with the short dimension perpendicular to the substrate. Therefore, it has been estimated based on the average aspect ratio of the larger nano-objects. The average sizes of all samples used in this study are listed in Table 1. The XRPD patterns of all the samples taken at room temperature indicate that the bulk and nanoparticles are isostructural with space group *P*4/*mmm* (Figure S1). In addition, all the diffraction peaks become broader when decreasing the particle size and show anisotropic peak broadening compatible with a shorter dimension of the crystals along the c-axis. As previously observed using electron microscopy, it can be safely assumed that the a and b-axis form the base and the c-axis goes along the short dimension of the platelets.[46] It is worth noticing that by using the reverse micelle technique, square-shaped particles are always obtained, which indicates that the growth along the c-axis, where the pyrazine ligands are situated (see Figure S2a) is inhibited to some extent by the surfactant, whereas the synthesis of the microcrystalline powder by fast precipitation (1.3 µm crystallites, which will be called bulk in the remaining of this article) leads to crystallites in the form of rectangular prisms with the c-axis as long dimension, indicating a different growth mechanism.

Table 1 Crystallite size of all the samples used in the study.(obtained by analysis of about 150 particles).

Length	Thickness	Length/Thickness*
32 ± 3 nm	5 ± 2 nm	7 ± 3
50 ± 10 nm	7 ± 4 nm	7 ± 3
142 ± 30 nm	25 ± 4 nm	6 ± 2.0
383 ± 90 nm	79 ± 10 nm	4.9 ± 1.7
563 ± 100 nm	53 ± 12 nm	11 ± 4
1.3 ± 0.3 µm	0.3 ± 0.1 µm	4 ± 2

*a/c for the submicrometric crystallites obtained by reverse micelle technique and c/a for the1.3 µm bulk material obtained by fast precipitation.

The thermal spin transition has been probed on the different samples by magnetic measurements (see Figure S2). The results obtained are in line with the previous reports, i.e., a decrease of the transition temperature and cooperativity is observed upon size reduction.[43-44]

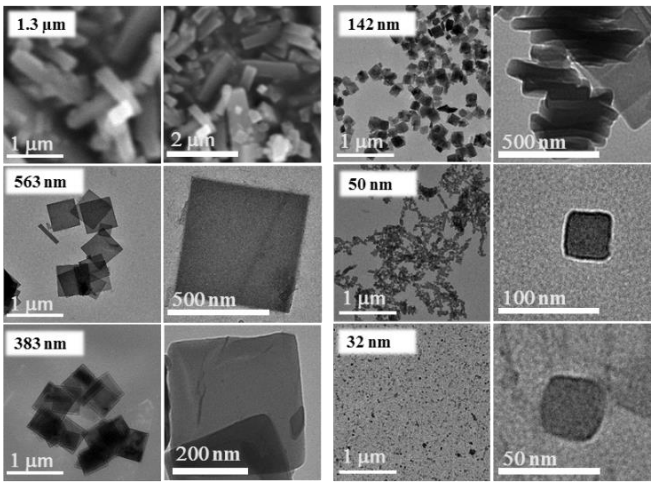

Figure 1 TEM image of the different [Fe(pz)Pt(CN)$_4$] samples

Photo-induced LS→HS spin conversion followed by XPRD.

In a first step, long-exposure high-quality patterns were recorded at 300 K and after cooling at 15 K with a Helijet (Figure S3). The corresponding unit-cell parameters determined by Pawley fits[47] between 4 and 14 degrees are given in Table 2. In all cases the samples stayed in the tetragonal space group *P*4/*mmm*. At room temperature the unit-cell volume of all the samples matches the value of the bulk material in the HS state, except for the 142 nm particles with an apparent remaining LS fraction calculated of around 13 % using the Vegard's law. When the samples are placed in the Helijet, resulting in very rapid cooling to 15 K, the unit-cell volumes of all the samples are slightly higher than the one of the bulk, indicating non-negligible remaining HS fractions (see Table 2). This is probably due to partial quenching of the HS state resulting from the very fast cooling in the Helijet, since both the optical absorption spectra at 10 K and the XRPD registered at 80 K after a slow cooling at 1 K/min indicate that the HS fraction at low temperature should be closer to 0 for these particles.[48]

The samples were converted to the HS state at 15 K by 532 nm laser irradiation through the light induced excited spin state trapping (LIESST) effect. For the XPRD experiments, the quantity of sample was optimised in order to obtain a quantitative photoexcitation of the whole sample with laser powers lower than 10 mW/mm^2. All results were compared to the ones obtained for the microcrystalline powder reported in a previous publication.[19] (See Experimental Section for more details on sample preparation, temperature control and irradiation conditions). The cell parameters after 5 minutes of irradiation are included in Table 2. Due to the thermal contraction along the c-axis, the value of the volume of the HS phase under irradiation is expected to be slightly lower than the one of the HS phase recorded at 300 K (Figure S4). Therefore, the unit-cell parameters after irradiation at 15 K are consistent with an almost quantitative LS→HS photoconversion.

HS→LS relaxation followed by XPRD.

The time evolution of the XRPD patterns during the HS→LS relaxation was then followed in the dark at 15 K. Figure 2 displays the time evolution of the (110) reflexion during the relaxation for all the samples. Overall, a shift of the peaks towards higher angle is observed, indicating a decrease of the unit-cell volume that is consistent with the HS→LS relaxation. A different behaviour is observed depending on the size of the crystallites. For the 32 nm, 50 nm and 142 nm samples, a shift of the (110) peak from lower to higher angles occurs during the relaxation while the peak intensity and linewidth remain almost constant. This behaviour indicates a progressive homogeneous increase of the LS fraction during the relaxation. In contrast, for the 383 nm and 583 nm particles, the evolution monitored by XPRD is more complex. At first, the (110) peak shifts towards higher angle and becomes asymmetric and less intense. This observation can be attributed to the formation of a distribution of mixed HS-LS phases. Concomitantly a peak situated at higher values of 2θ, whose position remains always the same, appears and gains in intensity. This peak corresponds to the formation of a pure LS phase. This behaviour is similar to the one previously reported for the bulk material.[19]

Table 2. Lattice-parameters *a* and *c* and unit-cell volume *V* of the different samples at 300 K and at 15K before and after irradiation.

Size (nm)	**32**	**50**	**142**	**383**	**583**	**1300**
300 K						
a / Å	7.420	7.427	7.385	7.434	7.435	7.435
c / Å	7.227	7.237	7.219	7.232	7.235	7.244
V / Å^3	397.89	399.19	393.71	399.67	399.95	400.50
γ_{HS}	0.95	0.97	0.87	0.98	0.98	1.00
15K dark						
a / Å	7.382	7.240	7.263	7.20	7.206	7.172
c / Å	7.117	6.839	6.864	6.82	6.817	6.770
V / Å^3	387.83	358.48	362.08	353.73	353.97	348.22
γ_{HS}	0.76	0.20	0.27	0.11	0.11	0
15K irr						
a / Å	7.417	7.401	7.420	7.429	7.423	7.438
c / Å	7.217	7.170	7.164	7.161	7.179	7.169
V / Å^3	397.01	392.74	394.42	395.22	395.57	396.62

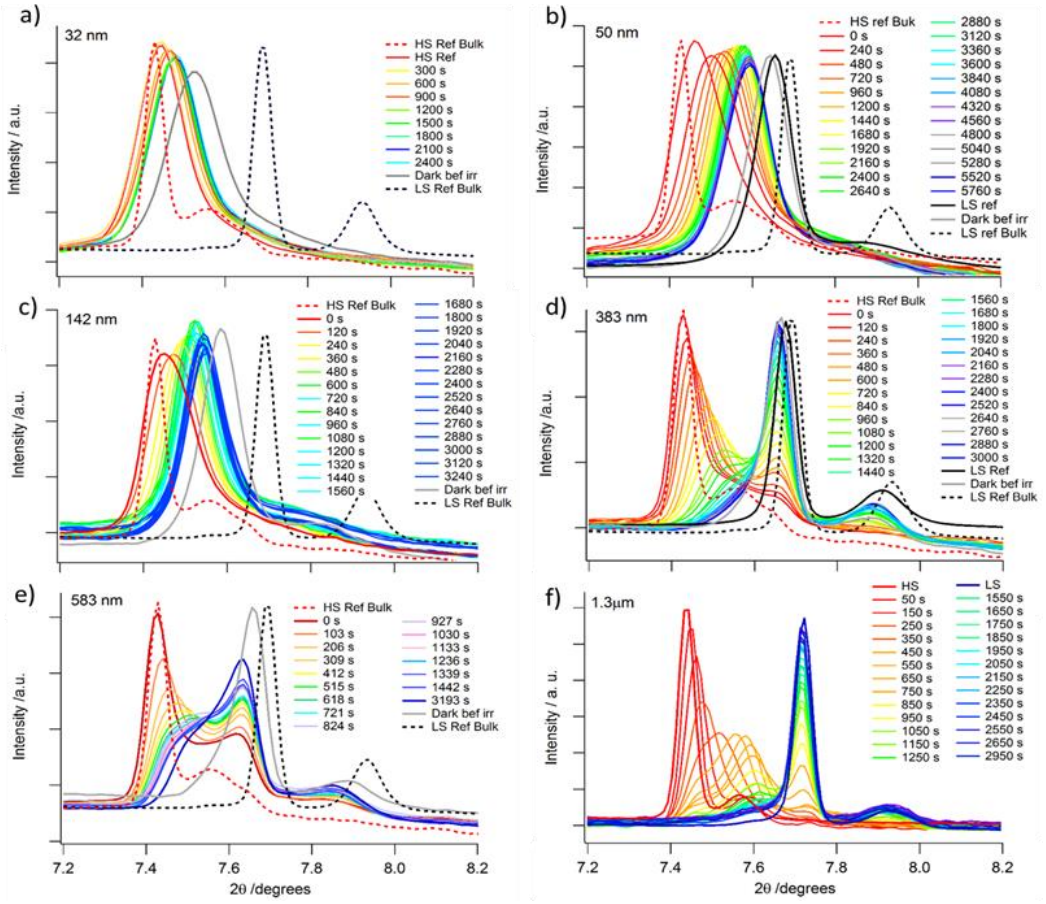

Fig. 2 Evolution of the XRPD pattern after irradiation at 532 nm with 7 mW/mm^2 around the (110) reflexion of all the [Fe(pz)Pt(CN)$_4$] samples used in this study at 15 K. The two-theta axes have been corrected so all the data are equivalent to data measured at λ = 0.6803 Å.

The full patterns were then modelled with Pawley refinements to closely analyse these variations. The details about the fitting parameters for all the samples at different relaxation times can be found in the Supporting Information, as well as examples of the fitting of the patterns for the 142 nm and 383 nm particles (Figure S5a and S5b). Before further discussion, some considerations for the fitting of all the samples should be highlighted. First, the quality of the data is limited by the short data collection time used during time-resolved experiments and the low amount of sample needed to achieve quantitative light conversion. Therefore, only the first part of the pattern (from 4 to 11° in 2θ) corresponding to the most intense diffraction peaks has been used. Then, the anisotropic line broadening makes it rather difficult to use a global peak shape for the entire pattern. Several anisotropic line broadening models have been tested but the best results are obtained by using an individual linewidth per peak. In addition, because the model is based on a rather high number of parameters to refine, some limits have been enforced during the refinement on the unit-cell parameter values and on the intensity ratio between the different peaks, since the structures of the HS and LS phases and thus these ratios are already known. Finally, in order to stabilize the refinement, a damping factor has been applied.

The variation of the unit-cell volume and of the integrated intensity of the different phases during the relaxation are shown in Figure 3 for all the samples (see Figure S6 for the variation of the *a* and *c* unit-cell parameters and the integrated full width at the half maximum). These parameters vary in a very different way depending on the size of the particles, in agreement with the above-described qualitative description of the (110) peak evolution:

- For the 383 nm and 583 nm particles, a model with two different phases: a mixed HS/LS phase and an almost pure LS phase, was used for the Pawley refinement. The peaks corresponding to the mixed HS/LS phase present an asymmetric shape, which was modelled using a split pseudo-Voigt function. The unit-cell parameters of this phase, corresponding initially to the pure HS state, evolve very slowly at the beginning of the relaxation and then decrease faster until their stabilization at values corresponding to HS fractions of 0.40 and 0.75 for 383 and 583 nm particles, respectively. The associated FWHM increases with time from around 0.05 - 0.07° to 0.15- 0.20°, depending on the sample, indicating that the distribution of spin states in this phase is getting broader during the relaxation process. On the other hand, the second phase, with unit-cell parameters corresponding to a pure LS phase, starts to appear after a few 100 s. The integrated intensities of the

corresponding Bragg peaks increase during the relaxation concomitantly with the decrease of the integrated intensity of the other phase. This behaviour, rather similar to the one previously evidenced with microcrystals, is consistent with random HS-LS relaxations at the early stages, followed by the nucleation and growth of a pure LS phase when a critical LS fraction is reached. This critical value can be evaluated to 0.02, 0.05 and 0.42 for 383, 583 nm and 1.3 ⍰m particles respectively. A smaller LS fraction is therefore required in order to observe nucleation-growth processes when the particle size decreases.

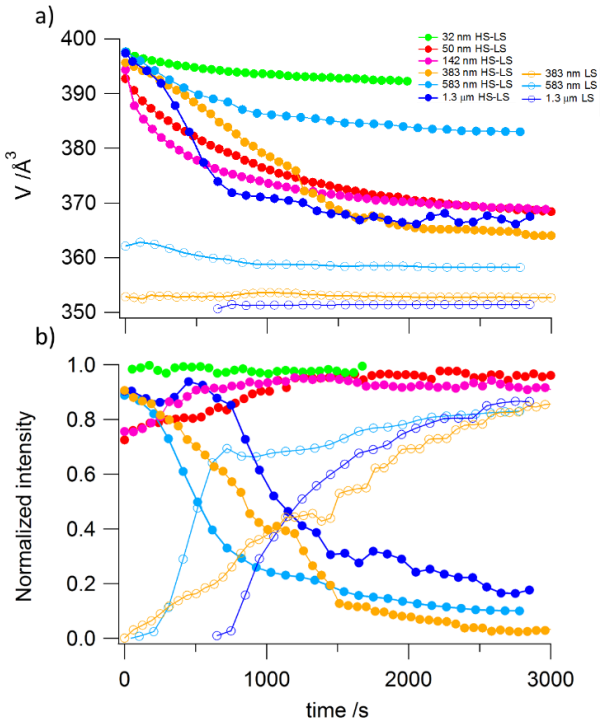

Fig. 3 Time evolution of a) the unit-cell volume and b) the integrated intensity of the (110) reflexion during the HS→LS relaxation after photo excitation with 532 nm laser at 7 mW during 20 minutes at 15 K of all the samples. Legend: 32 nm (green), 50 nm (red), 142 nm (pink), 383 nm (orange), 583 nm (clear blue) and bulk (dark blue). For the three last samples, two phases are present.: a mixed phase shown with filled circles and a LS phase shown with empty circles).

- For the 32 nm, 50 nm and 142 nm particles, a model with only one mixed HS/LS phase was chosen. The unit-cell parameters of this phase, initially corresponding to the pure HS one, decrease quite fast at the beginning of the relaxation, indicating a HS-LS relaxation. At the same time, the integrated intensity of the peaks remains almost constant. After approximately 500 s, the relaxation becomes infinitely slow and the corresponding unit-cell parameters indicate a large fraction of SCO centres remaining HS even after 3000 s. This phenomenon is even more accentuated in the case of the smallest particles (32 nm) for which the relaxation is even slower. Such behaviour indicates that for the smaller particles, the relaxation proceeds only through the random creation of LS centres everywhere in the material, without the formation of large clusters. The small increase in linewidth indicates only rather small fluctuations in the HS/LS ratio across the crystallites.

In order to quantify the evolution of the HS fraction as a function of the time during the relaxation, we assume that the population of each phase is proportional to the (110) diffraction peak intensity, since the sum of intensities is almost constant. The HS fraction can then be calculated using the following equation:

$$\gamma_{HS}(t) = \sum_{i=1}^{n} \frac{I_i(t)}{I_{tot}} \gamma_{HS}^{i}(t), \qquad (1)$$

where $\gamma_{HS}(t)$ is the HS fraction at time t, $I_i(t)$ is the (110) integrated peak intensity of the phase i at time t, I_{tot} is the total (110) integrated peak intensity and $\gamma^{i}_{HS}(t)$ is the HS fraction of phase i at time t. The HS fraction of each phase is obtained considering only the evolution of the unit-cell volume according to Vegard's law:

$$V_{HS}^{i}(t) = \frac{V_i(t) - V_{LS}}{V_{HS} - V_{LS}}, \qquad (2)$$

where $V_i(t)$ is the unit-cell volume at the time t, V_{HS} is the unit-cell volume of the HS state at 15 K (obtained under continuous irradiation) and V_{LS} is the unit-cell volume of the LS state at 15 K. As previously described, two phases (a pure LS and a mixed phase) are taken into account for the larger particles. For the mixed phase, asymmetric Bragg peaks are observed, corresponding to a distribution of solids with different HS/LS ratios. This peak is therefore decomposed as a sum of rectangles and the contribution of each rectangle is included in equation 1 (see Figure S7). The other phase is a pure LS phase whose integrated intensity is added to I_{tot} (See Appendix 1 in the Supporting Information for further information).

Figure 4 presents the time evolution of the HS fraction during the HS→LS relaxation at 15 K of all the samples obtained with equation 1. The behaviour of the relaxation curve is consistent with the different microscopic behaviours that we could identify directly by looking at the evolution of the powder pattern diagram.

In the case of the bigger samples (383 nm and 583 nm) sigmoidal relaxation curves are observed, which are similar to the previously studied relaxation on the bulk material. Such self-accelerated relaxations are consistent with the observed nucleation and growth process.

For the smaller samples (32 nm, 50 nm and 142 nm), the HS→LS relaxation curves show a behaviour which cannot be fitted exponentially and that becomes extremely slow after a given time. Such shapes are consistent with the observed random HS-LS relaxation process and surface effects. Moreover, a decrease of the relaxation rate is observed with the size reduction. This could be explained by the stabilization of the HS phase observed in the thermal spin transition when decreasing the particle size (see Figure S1).

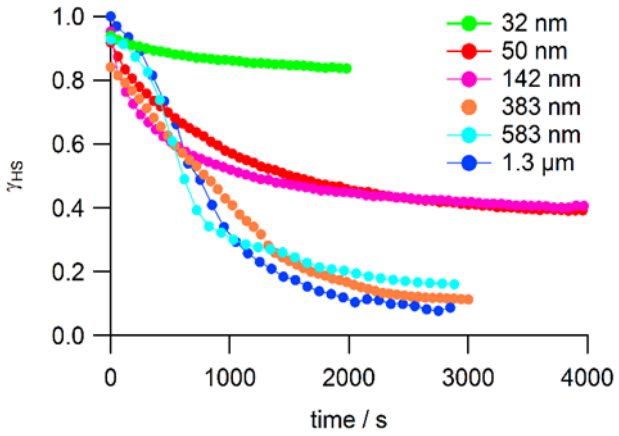

Fig. 4 Time evolution the HS fraction upon relaxation at 15 K, obtained by XRPD according to equation 1 for all the samples.

HS→LS relaxation followed by absorption spectroscopy.

The HS-LS relaxation after photo-excitation was followed for the smaller samples (32 nm, 50 nm and 142 nm) at different temperatures by absorption spectroscopy. For such purpose, the particles were dispersed on a Sapphire slide to get films of particles with reasonable optical quality. The absorption spectrum was first recorded at room temperature and then the sample was cooled down to 10 K, temperature at which the sample was irradiated at 532 nm, which corresponds to the maximum of the LS absorption band. After one minute of irradiation with a 10 mW/mm^2 laser power, the LS→HS conversion is almost quantitative. The maximum photo-induced HS fraction reached is around 0.9, due to the fast decay at the beginning of the relaxation. After the photo-excitation, the HS→LS relaxation was followed at 10 K. The experiment was then repeated systematically irradiating the sample at 10 K and heating it up to 20, 30 and 40 K before the relaxation, in order to check the effect of the temperature on the relaxation kinetics. Figure 5 presents the time evolution of the absorption spectra after irradiation of the 50 nm particles at 10 K (Figure 5a) and of the HS fraction after photo-excitation for all the above-mentioned temperatures (Figure 5b). For 50 nm particles, the relaxation at 10 K follows a comparatively fast decay during the first hour approximately, which starts to slow down when the HS fraction reaches 0.5 and then becomes infinitely slow, in such a way that the relaxation is not completed (γ_{LS} ~ 0.82) after 4 days. Similar results have been obtained for the 32 nm and 142 nm samples (Figure S8). The shape of the relaxation curves determined by optical measurements is in good agreement with the one obtained by XRPD. In addition, variable-temperature measurements confirm that the temperature at which all the XRPD experiments have been performed was 15 K.

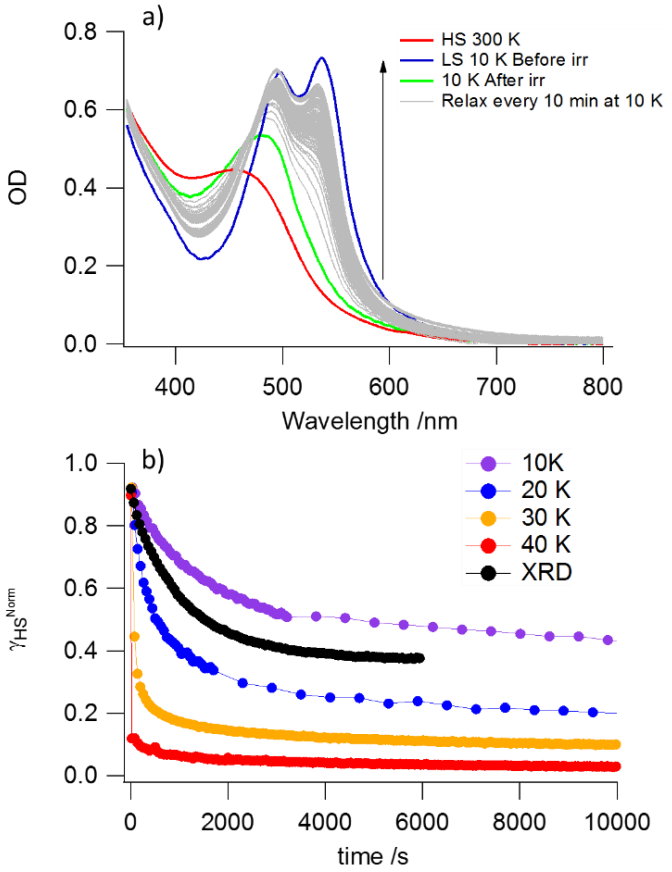

Fig. 5 a) Evolution of the optical spectra of the 50 nm nanocrystals deposited on a Sapphire disk after irradiation at 532 nm (around 10 mW/mm2) during 1 minute at 10 K and b) HS→LS relaxation curves at different temperatures determined from the evolution in time of the absorption spectra at 525 nm. The relaxation curve obtained from the XRPD at 15 K has been added in black.

Evolution of the diffraction patterns in the framework of the mechanoelastic model.

In order to understand the relation between the evolution of XRPD patterns and the cooperativity of the spin crossover process, we have performed extensive simulations using the mechanoelastic model,[30-31,48-51] in which the spin crossover centres are assigned to balls of different radius for the HS and the LS state, respectively, linked by springs having a spring constant k. The switching of a SCO centre from one state to another results in a volume change of that centre and consequently induces elastic forces on neighbouring springs, which propagates throughout the sample. The transition probabilities of SCO centres are then influenced by the local pressure p_i acting on every SCO centre, and, in the framework of an Arrhenius-type approach can be written as:

$$P^i_{HS\to LS} = \frac{1}{\tau}\exp\left(\frac{D - k_B T \ln g}{2k_B T}\right)\exp\left(-\frac{E_a - \kappa p_i}{k_B T}\right) \quad (3)$$

$$P^i_{LS\to HS} = \frac{1}{\tau}\exp\left(-\frac{D - k_B T \ln g}{2k_B T}\right)\exp\left(-\frac{E_a + \kappa p_i}{k_B T}\right), \quad (4)$$

here τ is a scaling constant, chosen so that the above probabilities are well-below unity at all temperatures, κ is a

scaling factor between the local pressure and the activation energy of the individual SCO centre, while E_a is the activation energy relative to a global reference state in which all the SCO centres are in the HS state. D is the difference in enthalpy between the two states, and g is the vibronic degeneracy ratio.[29] For the present simulations, if not stated otherwise, a rectangular shaped 2D sample, composed of 13982 SCO centres in a triangular configuration is used, which in real space corresponds to a 110x110 nm^2 sample for the typical unit-cell value of 1 nm^2 per SCO centre. The values of the parameters (κ, Δr_{HL}) considered in the simulations have been estimated from the experimental variation of the structure, ligand field strengths and bulk modulus during the spin transition.[30] The other parameters are specific to the studied system, [Fe(pz)Pt(CN)$_4$], and have been chosen in order to be physically relevant: ΔH = 4320x10^{-23} J (26 kJ/mol), ΔS = 14x10^{-23} J/K (84 J/K.mol or g = 22000) and k = 6 N/m. The corresponding simulated thermal spin transition occurs at 310 K ($T_c = \Delta H / k_B \ln g$) with a 14 K large hysteresis loop (see Figure S9) that is fully consistent with the experimental data.

The HS→LS relaxation curves at low temperature have been obtained by a Monte Carlo procedure[34] starting from a sample at γ_{HS} = 1 for different values of the spring or interaction constant k (Figure S10). Depending on the value of k, the shape of the relaxation curves changes: for low values they are almost exponential, for moderate values they become sigmoidal, while for strongly interacting systems, an almost discontinuous jump in the HS fraction can be observed. The cooperativity in the system is not only reflected by the shape of the relaxation curves but also by the macroscopic evolution of the system.

In order to model the experimentally observed XRPD patterns, we propose a method which allows the characterization of the cooperativity of the system without inspecting the individual clusters. The procedure is described in the following (see Figure 6):

(i) We select a rectangular area element composed of typically around 10x10 SCO centres;

(ii) This area element is then scanned across the whole crystallite in the x, y directions in steps of the unit-cell dimensions;

(iii) For each step we calculate the average HS fraction in the rectangle and we obtain a histogram for the number of rectangles for a given HS fraction;

(iv) This kind of histogram can be interpreted as being a direct representation of the evolution of an XRPD pattern during the HS→LS relaxation.

Using this scanning method, diffraction-like peaks for different values of k have been calculated (FigureS11). In the case of weak interactions (k = 0.1 N/m), the diffraction peaks stay Gaussian at all times while their centres move from 1 to 0, keeping almost the same height and width. This means that the fraction of HS SCO centres in all the scanning rectangles is similar, another way to say that switches occur almost randomly. For moderately strong interactions (k = 2 - 3 N/m), the distribution, especially around γ_{HS} = 0.5, becomes larger, which is a sign of larger inhomogeneities inside the sample. In the case of strong interactions (k = 4 - 8 N/m), the shape and width of the diffraction peaks dramatically change during the transition. They become very large in the middle of the transition, which is a sign of large variations in the HS fraction for different scanning rectangles, that is, in different regions of the sample. Sometimes, several local maxima appear, indicating nucleation and growth of clusters of different sizes (Figure S12). The simulated patterns with k = 6 N/m reproduce well the experimental data measured with the large particles (Figure 7a), which justifies the choice of this value for the further simulations.

In order to check the dependence of the cooperative effects on sample size, the scanning method has been applied to a second sample composed of only 864 SCO centres while keeping constant the value of elastic constant. In that case, a progressive shift of the diffraction peaks is observed along with a broadening for intermediate values of γ_{HS}, which qualitatively reproduces the experimental evolution of the diffraction patterns upon size reduction (Figure 7b). In addition, the size dependence of the corresponding HS-LS relaxation curves has been calculated. The simulated curves are in qualitative agreement with the experimental data (Figure S13) where less cooperative relaxations are observed for small particle sizes.

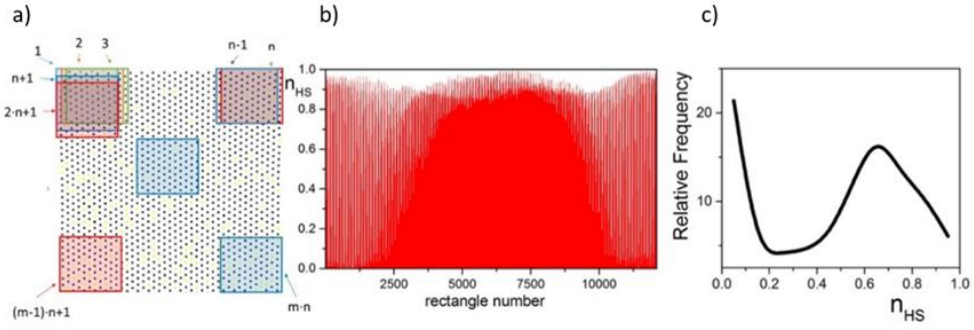

Fig. 6 Illustration of the data analysis procedure based on scanning different areas of the sample: a) selection of rectangular areas, b) histogram with average γ_{HS} values for every rectangle and **c)** like X-ray diffraction peaks.

The model provides a microscopic picture of how cooperative processes and size reduction influences the spin state switching mechanism. Indeed, the probability of a HS-LS transition during relaxation is determined by the competition between the gain in molecular Gibbs energy, defined as ΔG_{HL}

$= D - k_B T \ln g$ and the increase in elastic energy stored in the system due to distortions. In a given sample, the lowest elastic energy is obtained for nucleation starting from corners or edges. Therefore, switching and clustering in the bulk is less probable (Figure S14). As a consequence, in the case of large systems, a single cluster nucleation starting from the corner of the particle is expected. However, if one compares samples of different sizes, the ratio between the energy needed for switching a HS SCO centre situated in the bulk and a SCO centre in the proximity of a corner is several times smaller in the case of a smaller sample. Indeed, the increase of elastic energy due to the distortion during the transition in the bulk is higher for large particles because of the larger number of neighbouring sites. Therefore, larger fluctuations will be observed for smaller particles and several small clusters and/or homogeneous nucleation may be obtained, resulting in less cooperative spin transitions. In addition, in the case of nanocrystals, the presence of size and/or environment distribution of particles may increase the distribution of relaxation processes, resulting in a further broadening of the HS-LS relaxation curve.[48]

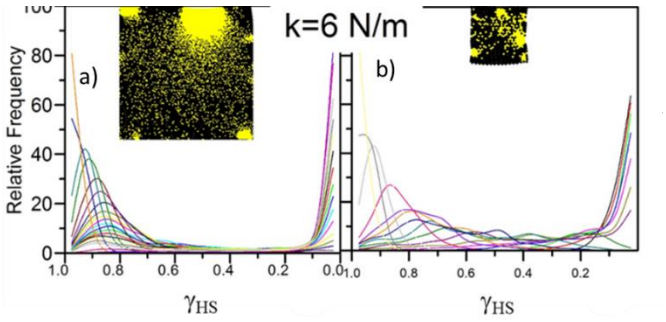

Fig. 7 Study of the like X-ray powder diffraction peaks with the size using the scanning method for k = 6 N/m and a system size of a) 13928 SCO centres and b) 864 SCO centres. The insets show the cluster at γ_{HS}= 0.7 with HS centres in black and LS centres in yellow.

Experimental methods

Sample preparation. $[Fe(pz)Pt(CN)_4]$ nanoparticles were prepared using the reverse micelle technique. The surfactant sodium bis(2-ethylhexyl) sulfosuccinate (NaAOT) was used to stabilize two different water-in-oil microemulsions: one containing $Fe(BF_4)_2 \cdot 6H2O$ and pyrazine (pz) and the other one $K_2[Pt(CN)_4]$ (see Table S1). The two microemulsions were then combined quickly. Alternatively, the $[Fe(pz)Pt(CN)_4]$ microcrystalline powder was obtained by mixing $Fe(BF_4)_2.6H_2O$ (67.4 mg, 0.2 mmol) and pyrazine (64 mg, 0.8 mmol) dissolved in 4 mL of water with a $K_2[Pt(CN)_4]$ solution (86.2 mg, 0.2 mmol) in 4 mL of water. In all cases the obtained precipitates were separated by centrifugation, washed with ethanol and dried at 127 °C during 12 h. Thermogravimetric analyses were performed before and after total water evaporation to be sure that the sample does not recover the water (see examples in Figure S15). Nevertheless, before each measurement, the samples were kept in the oven at 127 °C during at least 2 h to ensure that the sample was water-free.

X-Ray Powder Diffraction studies. The photo-induced spin transition was studied using the synchrotron-radiation-based XRD technique at the Swiss Norwegian Beamline at the European Synchrotron Radiation Facility in Grenoble (France). For the sample preparation, less than one milligram of $[Fe(pz)Pt(CN)_4]$ nanoparticles were deposited on a Kapton loop, which was placed in the diffractometer. Data were recorded using a Pilatus 2M detector (DECTRIS Ltd. Switzerland). The wavelength used was λ = 0.6803 Å for all the nanoparticle samples except the for 142 nm nanoparticles (λ = 0.6973 Å). For cooling the sample down, a helium cryostream (Oxford Instruments, Helijet) was used. In order to precisely monitor the temperature, a very small ruby crystal was placed together with the sample and the temperature was determined by calculating the ratio between the R1 and R2 emission bands of the ruby recorded on a Renishaw Raman spectrometer under irradiation at 532 nm with a CW Nd:YAG laser (See Figure S16 for more details). From these measurements, the exact temperature at the sample could be estimated to be 15 K.

Optical spectroscopy. The samples were first dispersed in acetone. The suspension was then deposited drop by drop on a circular Sapphire cover slide (10 mm diameter) while waiting until total evaporation of the solvent after the addition of each drop. This slide was placed on a copper plate with a previously drilled hole of about 3 mm in diameter and glued with silver paste. The plates were heated in the oven during 2h at 400 K and immediately transferred into the vacuum chamber of a closed-cycle cryostat (Janis-Sumitomo SHI-4.5) equipped with a programmable temperature controller (Lakeshore Model 331) in order to ensure that samples were unsolvated. Absorption spectra between 300 and 6 K were recorded with an optical spectrometer (Agilent Cary 5000).

Conclusions

This article evidences that $[Fe(pz)Pt(CN)_4]$ nanoparticles can be photo-excited at low temperature by irradiation with a 532 nm laser through the light-induced excited spin-state trapping effect. The evolution of the photo-induced HS fraction during the HS→LS relaxation was followed by different techniques. The results obtained by XRPD show that in the case of particles larger than 200 nm, the relaxation proceeds through a nucleation-growth based mechanism that is quite similar to the one observed in the bulk material, resulting in sigmoidal relaxation curves. In the case of particles smaller than 200 nm, random relaxations in the presence of inhomogeneities,

possibly caused by surface effects, are evidenced, giving rise to relaxation curve with a deviation from single exponential, presenting a slow tail at long delays. These results were confirmed by optical measurements. The mechanoelastic model was used in order to provide a direct visualisation of the system during the relaxation. It reproduces well the experimental evolution of the X-ray diffraction peaks during the relaxation and explains the evolution of the spin state switching mechanism upon size reduction by a balance between the particle size and the strength of cooperative interactions.

Despite many reports on the size-reduction effect on the spin state switching of spin crossover nanoparticles, this article provides the first experimental evidence of how the crystallites' size reduction can affect the spin state switching mechanism, which in this case evolves from nucleation-growth processes to random relaxation when the size goes below 200 nm. This result is of importance in order to get a better understanding of the dynamics of spin crossover compounds, which may help to design materials with optimised properties.

Conflicts of interest

There are no conflicts to declare.

Acknowledgements

We are grateful to the Swiss-Norwegian Beamlines (ESRF, Grenoble) for the provision of synchrotron beamtime. Financial support from the Swiss National Science Foundation (Grant No 200020_152780) is gratefully acknowledged. CE thanks CNCS-UEFISCDI Romania for a PCCE grant.

Notes and references

1. M. A. Halcrow and Editor, Spin-crossover materials: properties and applications, John Wiley & Sons Ltd., 2013.
2. P. Gütlich, V. Ksenofontov and A. B. Gaspar, Coord. Chem. Rev., 2005, 249, 1811-1829.
3. N. Negre, M. Goiran, A. Bousseksou, J. Haasnoot, K. Boukheddaden, S. Askenazy and F. Varret, Synthetic Metals, 2000, 115, 289-292.
4. P. Gütlich, A. Hauser and H. Spiering, Angewandte Chemie International Edition in English, 1994, 33, 2024-2054.
5. A. Hauser, J. Jeftić, H. Romstedt, R. Hinek and H. Spiering, Coordination Chemistry Reviews, 1999, 190–192, 471-491.
6. A. Hauser, Top. Curr. Chem., 2004, 234, 155-198.
7. Y. Garcia, V. Niel, M. C. Muñoz and J. A. Real, in Spin Crossover in Transition Metal Compounds I, eds. P. Gütlich and H. A. Goodwin, Springer Berlin Heidelberg, Berlin, Heidelberg, 2004, pp. 229-257.
8. E. König and K. Madeja, Chemical Communications (London), 1966, 61-62.
9. H. Peng, S. Tricard, G. Félix, G. Molnár, W. Nicolazzi, L. Salmon and A. Bousseksou, Angewandte Chemie International Edition, 2014, 53, 10894-10898.
10. T. Glaser, Angewandte Chemie International Edition, 2011, 50, 10019-10020.
11. P. Gütlich, Y. Garcia, Journal of Physics: Conference Series, 2010, 217, 012001.
12. P. Gütlich, H. A. Goodwin and Editors, Spin Crossover in Transition Metal Compounds I. [In: Top. Curr. Chem.; 2004, 233], Springer-Verlag, 2004.
13. S. Decurtins, P. Gütlich, C. P. Köhler, H. Spiering and A. Hauser, Chemical Physics Letters, 1984, 105, 1-4.
14. P. L. Franke, J. G. Haasnoot and A. P. Zuur, Inorganica Chimica Acta, 1982, 59, 5-9.
15. E. W. Müller, J. Ensling, H. Spiering and P. Guetlich, Inorganic Chemistry, 1983, 22, 2074-2078.
16. S. Decurtins, P. Gütlich, K. M. Hasselbach, A. Hauser and H. Spiering, Inorganic Chemistry, 1985, 24, 2174-2178.
17. P. Gütlich, A. B. Gaspar and Y. Garcia, Beilstein Journal of Organic Chemistry, 2013, 9, 342-391.
18. P. Guionneau, M. Marchivie, G. Bravic, J.-F. Létard and D. Chasseau, in Spin Crossover in Transition Metal Compounds II, Springer Berlin Heidelberg, Berlin, Heidelberg, 2004, pp. 97-128.
19. T. Delgado, A. Tissot, C. Besnard, L. Guénée, P. Pattison and A. Hauser, Chemistry – A European Journal, 2015, 21, 3664-3670.
20. M. Mikami, M. Konno and Y. Saito, Chemical Physics Letters, 1979, 63, 566-569.
21. J. Kusz, P. Gütlich and H. Spiering, Top. Curr. Chem., 2004, 234, 129-153.
22. M. Chergui and E. Collet, Chemical Reviews, 2017, 117, 11025-11065.
23. A. Ozarowski, Y. Shunzhong, B. R. McGarvey, A. Mislankar and J. E. Drake, Inorganic Chemistry, 1991, 30, 3167-3174.
24. L. Salmon, G. Molnar, D. Zitouni, C. Quintero, C. Bergaud, J.-C. Micheau and A. Bousseksou, Journal of Materials Chemistry, 2010, 20, 5499-5503.
25. C. Lochenie, K. Schötz, F. Panzer, H. Kurz, B. Maier, F. Puchtler, S. Agarwal, A. Köhler and B. Weber, Journal of the American Chemical Society, 2018, 140, 700-709.
26. F. L. Wimmer, Angew. Chem., Int. Ed. Engl., 1995, 34, 599-600.
27. P. Guionneau, Dalton Transactions, 2014, 43, 382-393.
28. H. Spiering, E. Meissner, H. Köppen, E. W. Müller and P. Gütlich, Chemical Physics, 1982, 68, 65-71.
29. C. Enachescu, M. Nishino, S. Miyashita, A. Stancu and L. Stoleriu, Phys. Rev. B, 2012, 86, 054114.
30. C. Enachescu and A. Hauser, Physical Chemistry Chemical Physics, 2016, 18, 20591-20599.
31. L. Stoleriu, P. Chakraborty, A. Hauser, A. Stancu and C. Enachescu, Physical Review B, 2011, 84, 134102.
32. A. Bousseksou, J. Nasser, J. Linares, K. Boukheddaden and F. Varret, J. Phys. I France, 1992, 2, 1381-1403.
33. F. Varret, S. A. Salunke, K. Boukheddaden, A. Bousseksou, E. Codjovi, C. Enachescu and J. Linares, C. R. Chim., 2003, 6, 385-393.
34. Y. Konishi, H. Tokoro, M. Nishino and S. Miyashita, Physical Review Letters, 2008, 100, 067206.
35. W. Nicolazzi, S. Pillet and C. Lecomte, Physical Review B, 2009, 80, 132102.
36. W. Nicolazzi and S. Pillet, Physical Review B, 2012, 85, 094101.
37. S. Pillet, V. Legrand, M. Souhassou and C. Lecomte, Physical Review B, 2006, 74, 140101.

38. W. I. F. David, K. Shankland, L. B. McCusker, C. Baerlocher and Editors, Structure Determination from Powder Diffraction Data. [In: Int. Union Crystallogr. Monogr. Cyrstallogr., 2002; 13], Oxford University Press, 2002.
39. A. Bousseksou, G. Molnar, L. Salmon and W. Nicolazzi, Chemical Society Reviews, 2011, 40, 3313-3335.
40. H. J. Shepherd, G. Molnár, W. Nicolazzi, L. Salmon and A. Bousseksou, European Journal of Inorganic Chemistry, 2013, 2013, 653-661.
41. A. Tissot, New Journal of Chemistry, 2014, 38, 1840-1845.
42. M. Mikolasek, G. Felix, W. Nicolazzi, G. Molnar, L. Salmon and A. Bousseksou, New J. Chem., 2014, 38, 1834-1839.
43. I. Boldog, A. B. Gaspar, V. Martínez, P. Pardo-Ibañez, V. Ksenofontov, A. Bhattacharjee, P. Gütlich and J. A. Real, Angewandte Chemie International Edition, 2008, 47, 6433-6437.
44. F. Volatron, L. Catala, E. Rivière, A. Gloter, O. Stéphan and T. Mallah, Inorganic Chemistry, 2008, 47, 6584-6586.
45. V. Niel, J. M. Martinez-Agudo, M. C. Munoz, A. B. Gaspar and J. A. Real, Inorg. Chem., 2001, 40, 3838-3839.
46. R. M. van der Veen, O.-H. Kwon, A. Tissot, A. Hauser and A. H. Zewail, Nat. Chem., 2013, 5, 395-402.
47. G. S. Pawley, J. Appl. Crystallogr., 1981, 14, 357-361.
48. T. Delgado, C. Enachescu, A. Tissot, L. Guenée, A. Hauser, C. Besnard, Phys. Chem. Chem. Phys., 2018, DOI: 10.1039/C8CP00775F.
49. C. Enachescu, L. Stoleriu, A. Stancu and A. Hauser, Physical Review Letters, 2009, 102, 257204.
50. L. Stoleriu, M. Nishino, S. Miyashita, A. Stancu, A. Hauser and C. Enachescu, Physical Review B, 2017, 96, 064115.
51. M. Nishino, C. Enachescu, S. Miyashita, P. A. Rikvold, K. Boukheddaden, F. Varret, Scientific Reports, 2011, 1, 162.